A sensitivity analysis to study the influence of surface integrity on the microcrack formation in high strength steels under compressive peak loading

[a,b]J. Nafar Dastgerdi, [a]F. Sheibanian, [b]H. Remes, [a]H. Hosseini Toudeshky

[a] Department of Aerospace Engineering, Amirkabir University of Technology, 424 Hafez Avenue, Tehran, Iran

[b] Department of Mechanical Engineering, Aalto University school of Engineering, P.O. Box 14300, FIN-00076 Aalto (Espoo), Finland

[b]jairan.nafardastgerdi@aalto.fi

Abstract

This paper provides a further understanding of the peak load effect on the damage mechanics and residual stress relaxation. The comprehensive numerical simulations using the finite element method are applied to take into account simultaneously the effect of the surface roughness and residual stresses on the crack formation in sandblasted S690 high strength steel surface under peak load condition. A ductile fracture criterion is introduced for the prediction of damage initiation and evolution. This study investigates especially the influences of compressive peak load, effective parameters on fracture locus, surface roughness, and residual stress on damage mechanism and the formed crack size. Results indicate that under peak load conditions, surface roughness has a far more important influence on microcrack formation than residual stress. Moreover, it is shown that the effect of peak load range on damage formation and crack size is significantly higher in comparison

with the influence of residual stress. It is found the crack size has been developed exponentially with increasing peak load magnitudes.

Keywords: Surface roughness, Residual stresses, Peak load, Finite element method, Micro crack formation

1 Introduction

The effect of surface treatments and different processing methods on the performance of the high strength steel under high peak stresses as single incidents or as a part of service loading is a major concern of the strength design and life prediction. The main affecting parameters describing the surface integrity are surface roughness, residual stress, and material properties in the surface layer. These parameters can vary separately according to the manufacturing procedures and machining conditions [1-3]. Therefore, the influences of these affecting parameters should be investigated on the performance and failure damage mechanism of high strength steels in the real engineering applications.

It has long been recognized that fatigue cracks generally initiate from the free surface and the local microscopic stress and strain concentration at the surface defects are significant factors for crack initiation and propagation [4-7]. Surface roughness is an important index to describe surface microtopography and it has a crucial effect on fatigue life [8-9], thus the effect of surface roughness on fatigue performance has been an intensive research area for several years and numerous researches have studied the effects and function mechanism of

surface roughness caused by various surface processing methods on the fatigue behavior of various materials [10-14]. Despite considerable advances in understanding the influence of surface roughness on fatigue performance of different kinds of materials, the role of surface roughness on the crack initiation and damage mechanism under peak load e.g. as an initial step before fatigue loading is poorly understood. Moreover, the effects of residual stress and material properties in the surface layer are still unclear simultaneously considering the impact of surface roughness effect on the crack formation and failure mechanism.

However, some researchers have investigated experimentally the effect of surface integrity on fatigue strength of high strength steels [15-17]. They have provided a comprehensive overview of the effect of these parameters on fatigue strength; although it is not possible to exploit enough understanding about the effect of surface roughness, hardness, and residual stress on failure mechanism, crack initiation, and propagation under cyclic loading for high strength steel materials. Therefore, predicting structure fatigue strength with new manufacturing processes and machining parameters is not possible except by performing new time-consuming and expensive fatigue tests. A better model encompassing the detailed characteristics of the surfaces with all affecting parameters is expected to capture the failure mechanism over a broad range of conditions. Thus, it is imperative to investigate the combined effect of surface integrity parameters on the damage mechanism and micro-cracking of engineering components under peak loads as the focus of this study.

Ductile fracture has been extensively studied for modelling and assessing the failure mechanisms of materials and structures especially metals (advanced high strain steel, aluminum alloy, titanium alloy, magnesium alloy, etc.) in different engineering practices using various proposed ductile fracture criteria [18-21]. These criteria were developed based

on various assumptions, hypotheses, or experimental observations of ductile fracture. The phenomenological ductile fracture criterion developed models for the prediction of the fracture process such as the crack initiation, propagation and failure mechanisms [22-24]. In order to implement these ductile fracture criteria to surface integrity analysis, the new finite element (FE) modeling approach was developed recently by the authors. The developed approach fully captures the complexity of the surface roughness using two-dimensional actual surface topography and the influence of residual stress by introducing global layer-wise modeling with constant temperature in each layer fallowing the estimated residual distribution [25]. The micro-mechanism motivated phenomenological damage model has been applied for predicting the ductile fracture initiation in the space of stress triaxiality and equivalent plastic strain [26]. The ductile fracture criterion is calibrated for the prediction of fracture locus with an inverse numerical-experimental approach to obtain the material constants in the criterion [25]. Although the approach is successfully calibrated with experiments, it is not yet applied for systematic analysis of the surface integrity effects.

Since surface integrity includes several influencing factors, in addition to experimental observation numerical simulation is required to reveal the main affecting factors. For instance, compressive loads tend to relax compressive residual stresses in proportion to their magnitude. Relaxation due to a single peak load is typically considered more effective than gradual cyclic relaxation [27-28]. As residual stress relaxation depends on the relationship of the local stresses and the local yield strength [29], surface roughness as an affecting parameter on the local stress concentration influences the relaxation behavior. It is unclear under what conditions does residual stress relaxation occur, or what is the impact of residual stress distribution on the crack formation and damage mechanism. It is well known that

residual stress relaxation is a complex phenomenon [30]. Therefore, the integration of residual stress in predictive modeling calculation, without considering their relaxation during operation, leads to an inaccurate prediction for the trustworthiness and reliability of the components and structures. This paper provides a further understanding of the influence of compressive peak load on the microcrack formation, crack size, and residual stress state of sandblasted high strength steels. The peak load effect on residual stress distribution has been studied and further analysis has been carried out to investigate the influences of peak load, effective parameters on fracture locus, and residual stress on damage mechanism and the crack size.

2 Materials and methods

2.1 Characteristics of sandblasted high strength steel surface

In this study, the sandblasted 690 high strength steel plate specimen with a plate thickness of 15 mm is considered. In this case, the previous experimental investigations provide well-described roughness measurement, residual stresses, and material properties [25]. The surface roughness measurements were carried out according to SFS-EN ISO 4288 [29], and the size of the surface profiles is defined for the rolled plate. The surface contour is depicted in Fig. 1. The elastic properties of the material are described by Young's modulus of $E = 210$ GPa, Poisson ratio of $\nu = 0.3$. Due to the complexity of the surface topology, high local stresses are expected to occur at the surface. To evaluate the effect of local plasticity on the near surface stress fields, the von Mises yield criterion is utilized in the simulations assuming associated plastic flow and isotropic hardening.

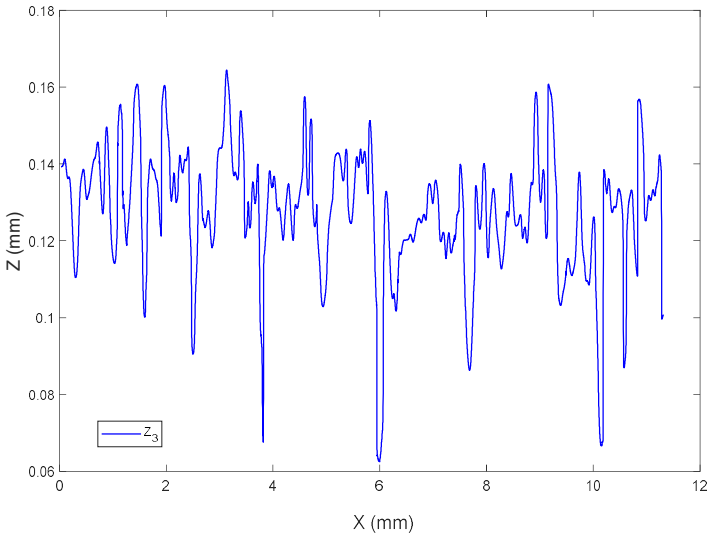

Fig. 1. Profile of the surface roughness [25].

In this study, the estimated through-thickness residual stress distribution with the maximum stress value (-80 MPa) at the surface [1] is employed. This distribution is obtained from the strain-gage hole drilling measurements for sandblasted steel samples [30]. Furthermore, to investigate the compressive residual stress effect on microcrack formation and crack size, the residual stress value at the surface is increased from -80 MPa to -320 MPa as reported experimentally for the grinding manufacturing process of 690 high strength steel plate [1].

2.2 Ductile fracture criterion

The micro-mechanism inspired phenomenological damage model described in [26] using fracture strain dependent on stress triaxiality is employed for the evolution of damage in this simulation. The damage model and calibration approach have been explained by details in Ref. [25], also shortly presented in this section to describe the physical basis and affecting parameters on numerical simulations carried out in this paper.

The criterion is constructed with consideration of damage accumulation induced by nucleation, growth and shear coalescence of voids [26], which has a form of

$$\left(\frac{2\tau_{max}}{\bar{\sigma}}\right)^{C_1} \times \left(\frac{\langle 1+3\eta \rangle}{2}\right)^{C_2} \times \bar{\varepsilon_f} = C_3 \qquad \langle x \rangle = \begin{cases} x & \text{when } x \geq 0 \\ 0 & \text{when } x < 0 \end{cases} \tag{1}$$

The model is based on the microscopic analysis of ductile fracture where void nucleation is described as a function of the equivalent plastic strain, the void growth is represented as a function of the stress triaxiality as $1 + 3\eta$, and void coalescence is controlled by the normalized maximal shear stress denoted as $\tau_{max}/\bar{\sigma}$. The effect of nucleation, growth, and coalescence of voids is controlled by the two calibration exponents: C_1 and C_2. The material constant C_3 is equal to the equivalent plastic strain to fracture in uniaxial tension. Although the model can describe these different phenomena, the reason why we preferred this criterion is that the shape of the fracture locus can be easily controlled with the three material constants. Furthermore, this equation gives the fracture strain for the full range of stress triaxiality.

Ideally, the input fracture criterion $\bar{\varepsilon_f}$ in Eq. (1) should be determined based on tests covering the full stress triaxiality range. For instance, in the study where the fracture model was proposed [26] the material constants C_1, C_2 and C_3, were obtained by fitting a curve to the experimental results. The same approach is used, but only uniaxial tension test data together with single peak load tensile are utilized. The input fracture criterion in the uniaxial tension range is calibrated based on calculated equivalent plastic strain at fracture initiation, failure strain $\bar{\varepsilon_f}$. The $\bar{\varepsilon_f}$ at uniaxial tension $\eta = 1/3$ gives the value for material constant C_3. This is calculated using an approach that first computes true stress-strain curve of S690 high strength steel under uniaxial loading and then the defined the true stress-strain curve has been implemented in FE simulation using a UMAT subroutine to calculate the equivalent von Mises plastic strain at fracture initiation [25].

To provide a full-range true stress-strain ($\sigma_t - \varepsilon_t$) curve of S690 high strength steel under uniaxial loading, the instantaneous area method has been employed to analyses the data provided from a digital imaging correlation technique. This technique has been adopted to measure deformation fields of steels coupons during the entire deformation ranges. Using this method, the constitutive model of the S690 high strength steel materials is proposed as follows to calculate true strain [31]:

$$\sigma_t(\varepsilon)\begin{cases} \sigma_t = E\varepsilon_t & for\ \varepsilon_t \le \varepsilon_y \\ \sigma_t = f_y \times \left[1 + 3 \times 10^{-3} \times (\varepsilon_t/\varepsilon_y - 1)\right] & for\ \ \varepsilon_y \le \varepsilon_t \le 6\varepsilon_y \\ \sigma_t = f_y \times \left\{1.015 + 0.1 \times \left[1 - 0.01 \times (0.6\left(\frac{\varepsilon_t}{\varepsilon_y} - 6\right) - 10)^2\right]\right\} & for\ 6\varepsilon_y \le \varepsilon_t \le 15\varepsilon_y \\ \sigma_t = f_y \times \left\{1.094 + 0.1 \times (\frac{\varepsilon_t/\varepsilon_y - 15}{100})^{0.45}\right\} & for\ 15\varepsilon_y \le \varepsilon_t \le 130\varepsilon_y \\ \sigma_t = f_y \times \left\{1.2 - 0.09 \times [(\frac{\varepsilon_t}{\varepsilon_y} - 130)^{1.1}/340]\right\} & for\ 130\varepsilon_y \le \varepsilon_t \le 1.2 \end{cases} \quad (2)$$

where $E = 210$ MPa.

Utilizing the proposed approach, the value for material constant C_3 is 1.2. Then different values for C_1, C_2 have been set based on the common range ($1 < C_1 < 8$ and $0 < C_2 < 1$) for these parameters [26]. Using an inverse numerical-experimental approach proposed by the authors, C_1, C_2 can be calibrated in such a way that FE simulation for pre-notched specimens with ductile damage can predict the micro-crack observed from SEM images in the vicinity of the notch under peak load conditions [25]. This new special approach is employed in this study and the constructed fracture locus using this calibration approach with the material constants $C_1 = 4, C_2 = 0.01, C_3 = 1.2$ has been utilized further in the FE simulation as shown in Fig. 2. Moreover, the sensitivity analysis on the effect of C_2 as the most affecting parameter on the micro-crack formation and crack length utilizing varied

fracture locus will be carried out. Figure 2 additionally shows the examples of calibrated fracture locus for different values of C_2.

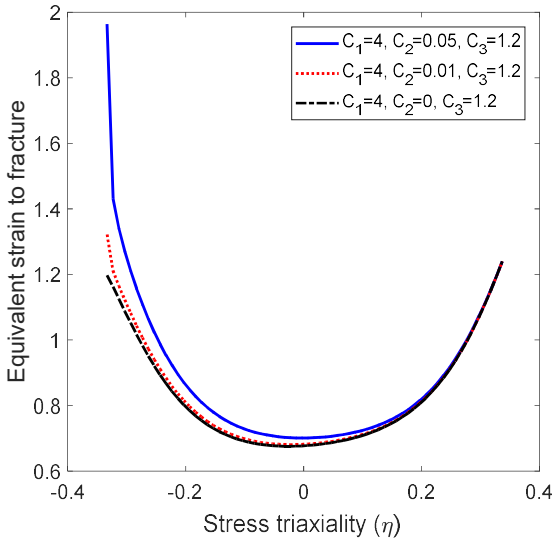

Fig. 2. Fracture locus for High strength steel 690.

2.3 Numerical simulation

The FE model was built using the two-dimensional real surface contour of the specimen measured by profilometry to capture the complexity of the surface roughness as depicted in Fig. 3. The final dimension of the model is taken as $31.1\ mm \times 11.28\ mm \times 15\ mm$. The element mesh is refined in the micro-defect root to be as small as possible being still valid for continuum mechanics. Thus, the minimum element size is defined as three times the average grain size of the material, equating to roughly 10 μm for the studied steel. The element type for the micro-defect root area, where material damage and crack formation occur, is four nodes with reduced integration to have robust numerical simulation for large strains and geometrical non-linearity.

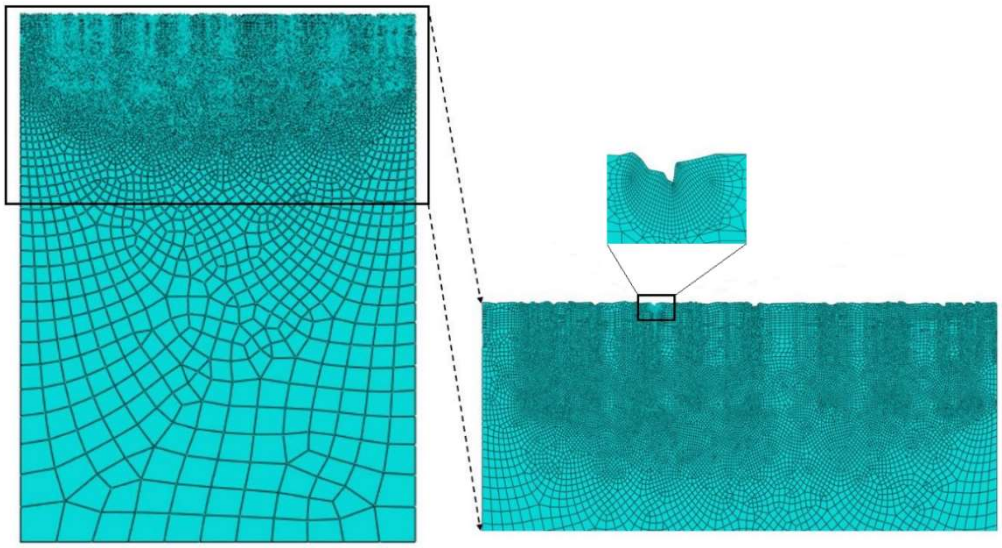

Fig. 3. Two-dimensional real surface topography model and local mesh [25].

The residual stress effect has been considered by proposing the layer-wise global modelling with constant temperature in each layer following the estimated residual distribution. In Fig. 4a, the measurement-based residual stress distribution is plotted as a solid smooth line, while the stepwise continuous lines represent the discontinuous residual stress distribution used in the layer-wise FE model. Figure 4b shows the applicability of the proposed modelling approach in defining the layers with constant temperatures using the estimated through-thickness residual stress distribution.

In this modelling approach, several layers are created in the FE-model and the residual stress distributions are introduced to the FE analysis as temperature fields. The field distribution, field magnitude, and thermal expansion coefficient determine the temperature field. In the present study a thermal expansion coefficient of $\alpha = 1.2\times10^{-5}$, which is typical for steel, is used. The temperature field is applied to the initial undeformed mesh.

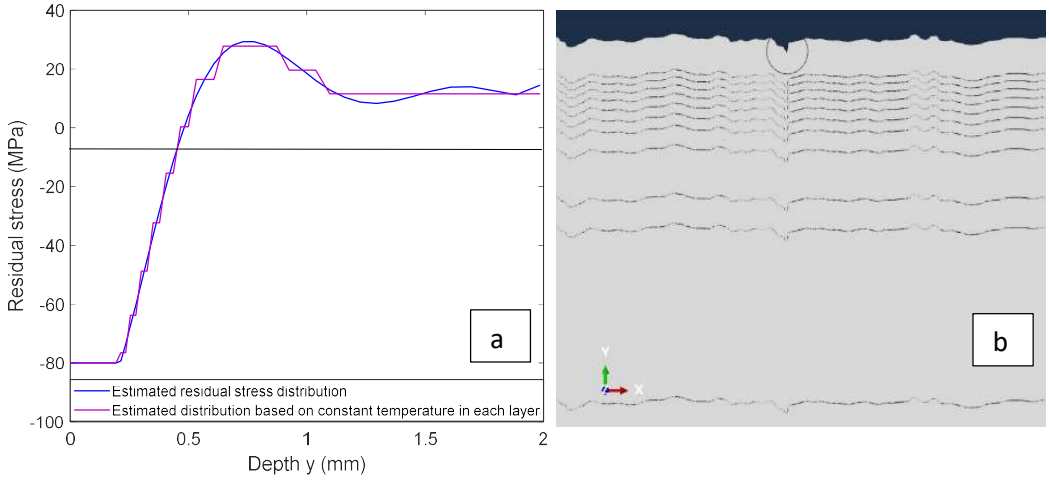

Fig. 4. (a) Continuously estimated residual stress distribution (solid line) and discontinuously estimated residual stress distribution with constant values in each layer (stepwise continuous line), (b) layer-wise global modeling [25].

FE simulations are carried out on the model according to the loading conditions as shown in Fig. 5 with single compressive peak load. The specimen is subjected compressive loading to relax or redistribute the residual stress. The compressive peak load is around the yield stress (-1.1 S_y) similar to the situation that the ship is launched or is in severe weather conditions. Then one tensile load cycle is considered for this material like the typical fatigue loading in service.

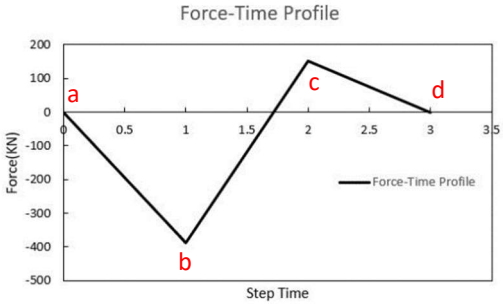

Fig. 5. Loading condition in one cycle [25].

3 Results and discussion

The sensitivity analysis has been carried out for surface roughness, residual stress, and peak load effects. Firstly, the residual stress effect on the damage initiation, evolution, and crack formation has been investigated. Moreover, the peak load effect on residual stress

distribution, and relaxation behaviour has been studied. Secondly, the influences of peak load and affecting factors on fracture locus have been examined.

3.1 Influence of residual stress on micro-crack formation

Figure 6 shows the damage initiation, evolution, and cracks formation based on element deletion for the most critical micro-notch caused by the surface roughness using ductile fracture criteria without residual stress effect. In Fig. 7, the residual stress of – 80 MPa has been additionally considered in the FEM using layer-wise global modelling. The result in terms of damage i.e. formed crack size is very similar to both analysis cases done without and with residual stresses. This result has raised an important question and proved that further understanding and analysis are required to determine the effect of residual stress on the damage mechanism. For this purpose, the first element exactly below the critical notch has been observed during the damage mechanism with and without residual stress effect.

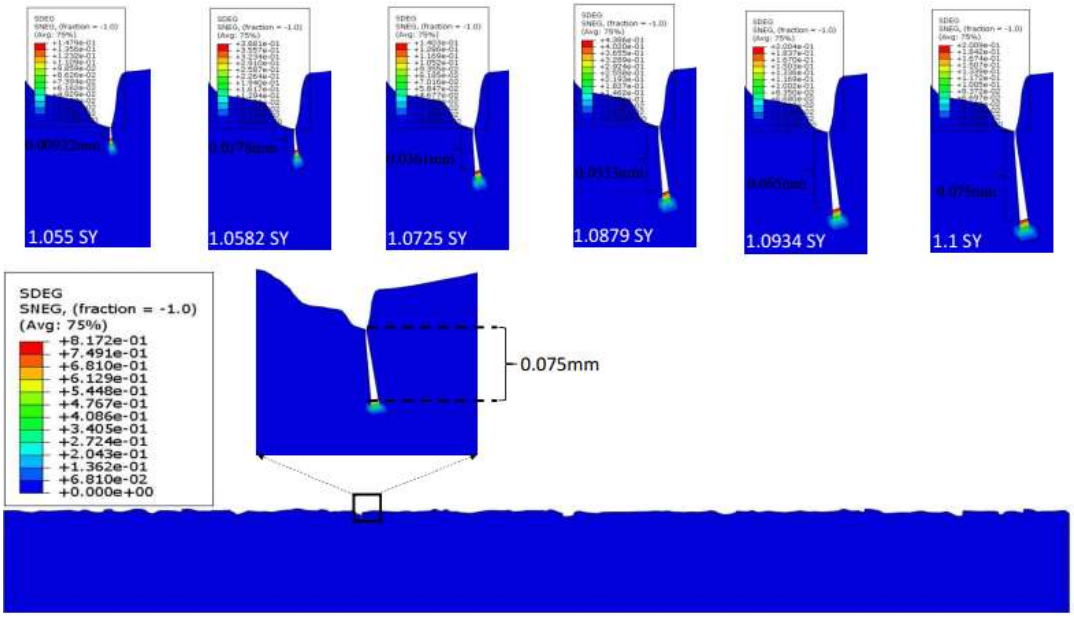

Fig. 6. The damage initiation, evolution and crack formation for the most critical micro-notch at the surface without residual effect.

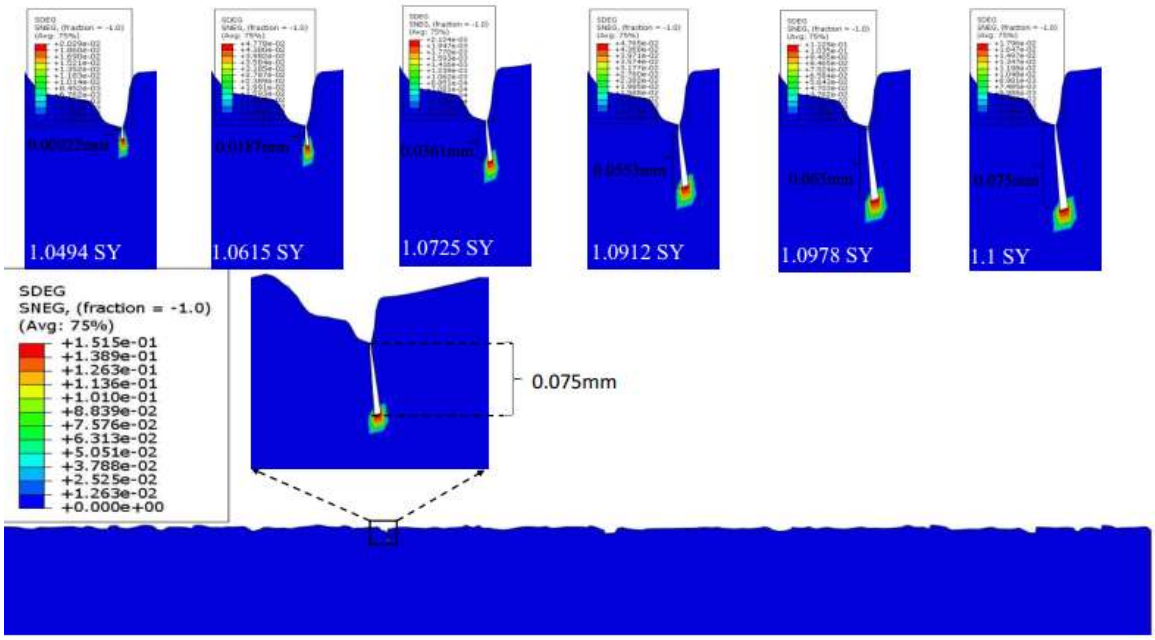

Fig. 7. Crack formation for the most critical micro-notch at the surface with residual effect -80 MPa.

Figure 8a shows the stress values versus step time for this element with and without residual stress effect. The loading step time is considered for the compression peak load as depicted in Fig. 8b from a to b point. In the case that the residual stress effect is considered, there is a pre-step in our modeling that we use to define the residual stress. In this figure, the step time from -1 to 0 presents this pre-step. It can be seen that the presence of residual stress as defined based on the temperature field in the pre-step causes that the element experienced stress value around -327 MPa at the beginning of the loading step while in the other case without residual stress effect, the stress values in the element start from zero at the beginning of the loading step. It can be seen after around 0.3 of the time step the element in both cases with and without residual stress is experiencing the same stress values. When equivalent strains, defining the element failure and removal, are also similar then we cannot expect differences in the damage initiation and crack formation for these two cases.

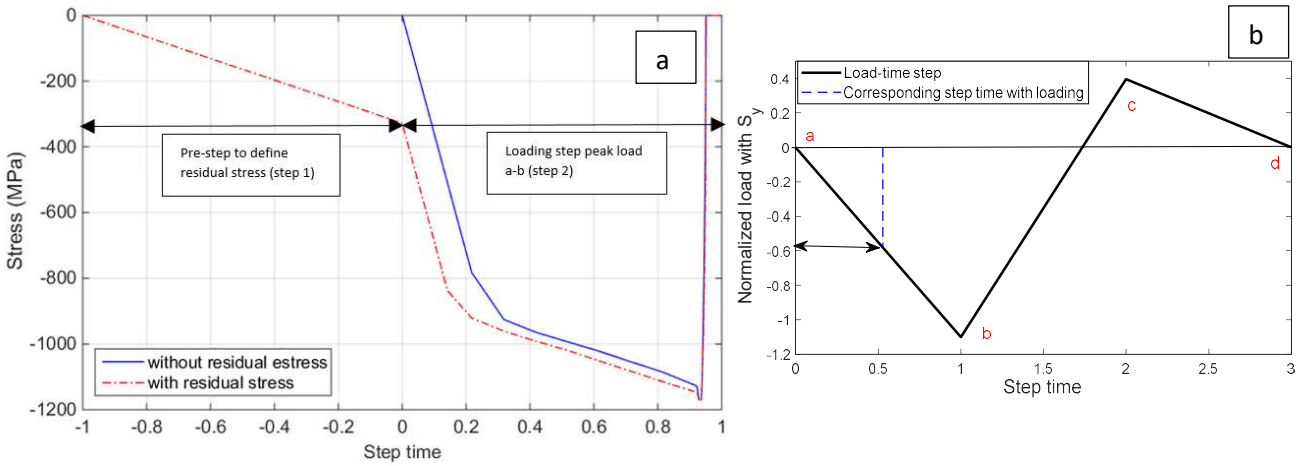

Fig. 8. The stress values versus step time for the first element exactly below the critical notch without and with -80 MPa residual stress.

This phenomenon might be related to the residual stress relaxation occurring under this loading condition. The initial residual stress field inherent in or induced in the finished product may not remain stable during residual stressed component operation life. These residual stresses may decrease and redistribute, and this reduction is called relaxation. Relaxation takes place, mainly, when the sum of the external and residual stress exceeds the yield stress of a material locally. When externally applied load is superimposed on residual stresses, unexpected deformations and failure of the components can occur. These residual stresses are not constant but are relaxed or redistributed during in-service. Generally, a large relaxation would be expected in the high-stress region similar to what happened in this study with $-1.1\ S_y$ external load value. Figure 9 depicts the stress distribution at different step time of the loading. It can be seen that the multi-layer residual stress distribution is disappeared at step $-0.58\ S_y$ of the loading or around the middle of the loading step from a to b point as depicted in Fig. 8b.

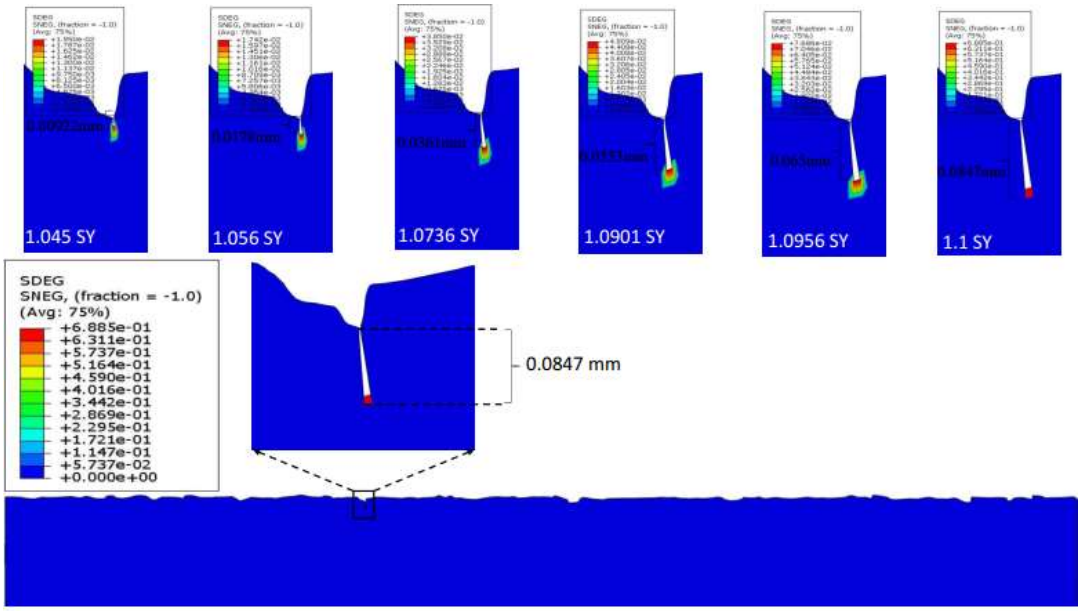

Fig. 9. Stress distribution at different step time of the loading with stress residual effect -80 MPa.

For further analyses, the residual stress value is increased from -80 MPa to -320 MPa to investigate the residual stress effect on the fatigue damage mechanism more precisely. With increased value for the residual stress, it can be seen there are differences between with and without residual stress cases in damage mechanism and the length of the crack as shown in Fig. 10 in comparison with Fig. 6; however, the crack size is not significantly increased, i.e. from 75 μm to 84.7 μm. For higher residual stress (-320 MPa), the notch stress value reaches the yield stress of the material already during the pre-step and the stress value at the beginning of the loading step time is around -946 MPa; see Figure 11.

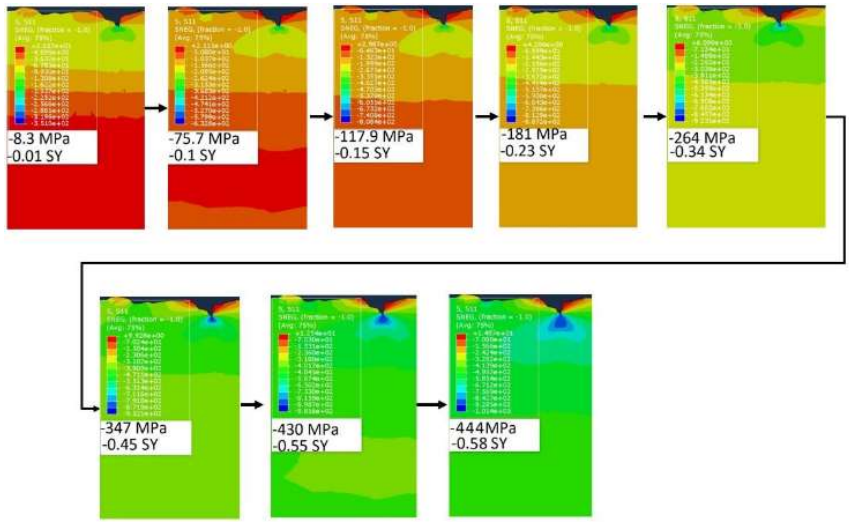

Fig. 10. Crack formation for the most critical micro-notch at the surface with residual effect -320 MPa.

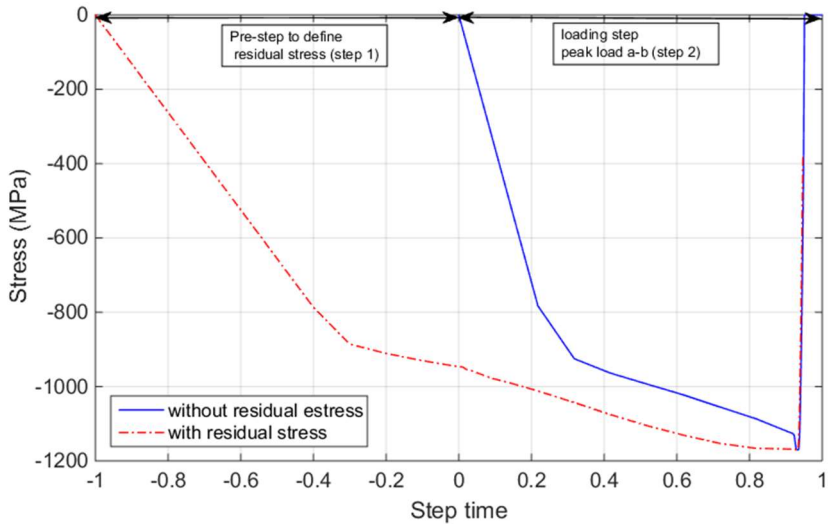

Fig. 11. The stress values versus step time for the first element exactly below the critical notch without and with -320 MPa residual stress.

The stress distribution at different step time of the loading for this case with -320 MPa residual stress is shown in Fig. 12. It is observed that the multi-layer residual stress distribution remains effective at step 9 of the loading corresponding to $-0.45\,\sigma_y$ of the loading; however, it is relaxed after some more step time corresponding to $-1\,\sigma_y$ of the loading. It can be concluded that the residual stress relaxation rate, in this case, is lower in

comparison with the other case with lower residual stress value (-80 MPa) while elements have not experienced plastic deformation in pre-step with residual stress effect at the beginning of the loading step. These results also clarify the reason for further crack formation in this case with a higher value of residual stress in comparison with a lower value.

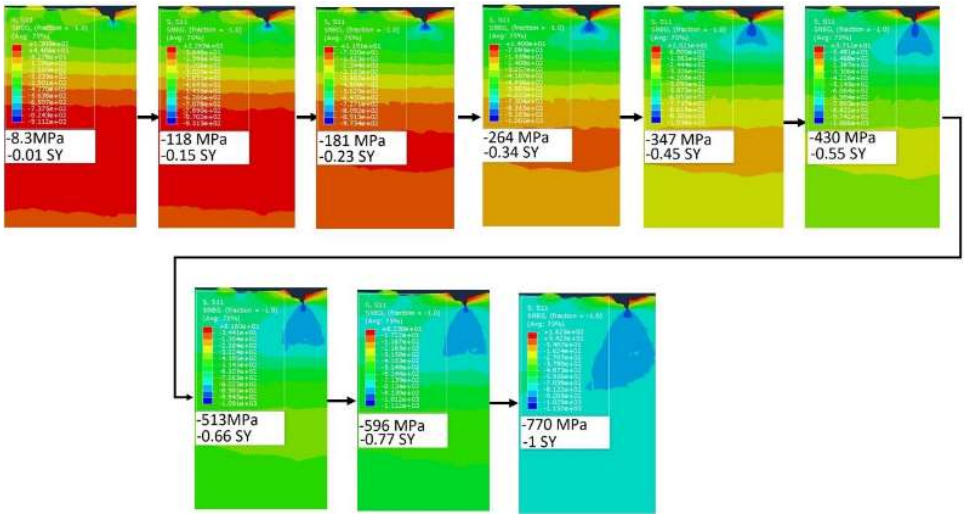

Fig. 12. Stress distribution at different step time of the loading with stress residual effect -320 MPa.

Figure 13 shows the crack formation (crack length) as a function of normalized stress value with the nominal yield strength of the material with different residual stress values, -80 MPa and -320 MPa. The slope of crack length versus load is quite similar for both cases; however, this slope is higher for residual stress -320 MPa at the final step of loading.

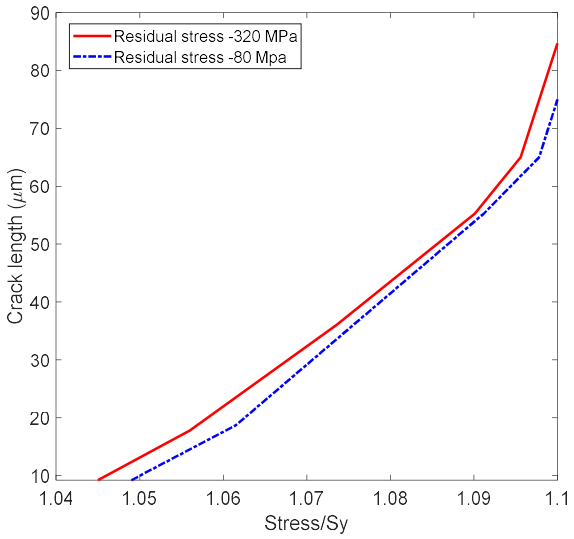

Fig. 13. Crack length versus normalized stress with nominal yield strength of the material with different residual stress values (-80 MPa and -320 MPa).

3.2 Influence of peak load on residual stress relaxation

To study the effect of peak load values on the residual stress relaxation and distribution, further analyses have been carried out in the case that there is not overload while residual stress effect is considered. Therefore, the load history, in this case, is a-c-d as shown in Fig. 8b. Figure 14 depicts the stress distribution at different step time of the loading. It is found that the residual stress remains effective at the end of the loading step; however, it is redistributed during the loading step time. Moreover, the predicted residual stress distribution at the beginning of loading and the stress distribution at the end of the loading step is shown in Fig. 15 along the path below the critical notch. The predicted stress experiences higher values close to the notch tip due to stress concentration factor and large localized plastic deformation; however, the residual stress remains effective at the end of the loading step

without residual stress relaxation. It can be concluded that in the presence of residual stress the overload value affects the residual stress relaxation rate and distribution.

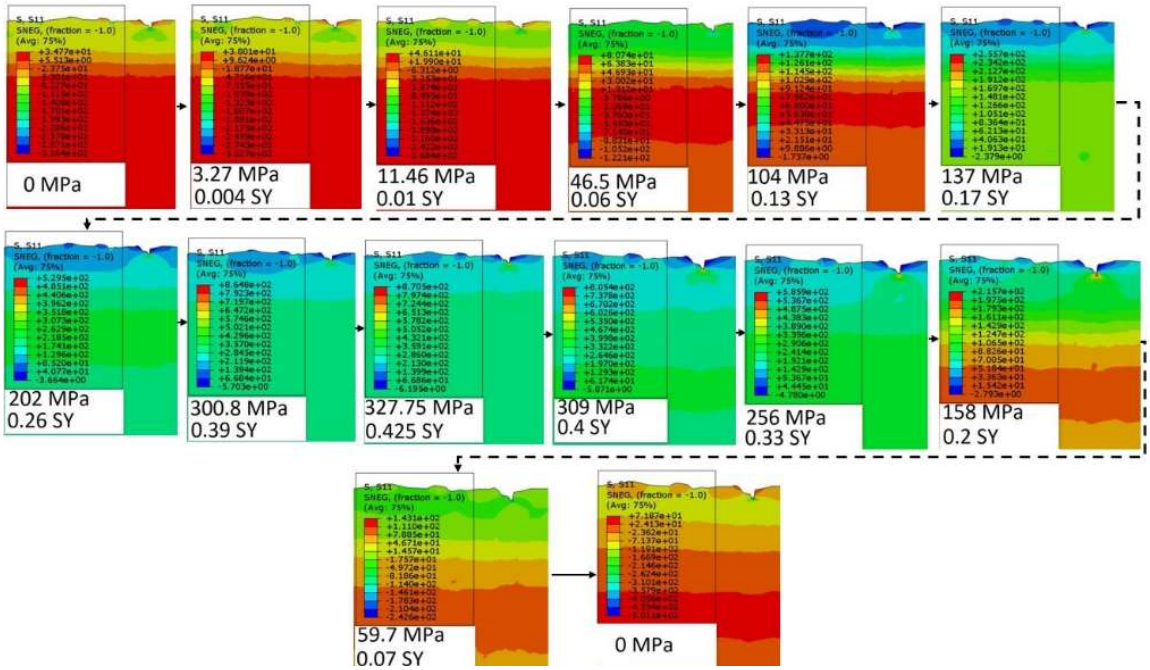

Fig. 14. The stress distribution at different step time of the loading without peak load and with stress residual effect.

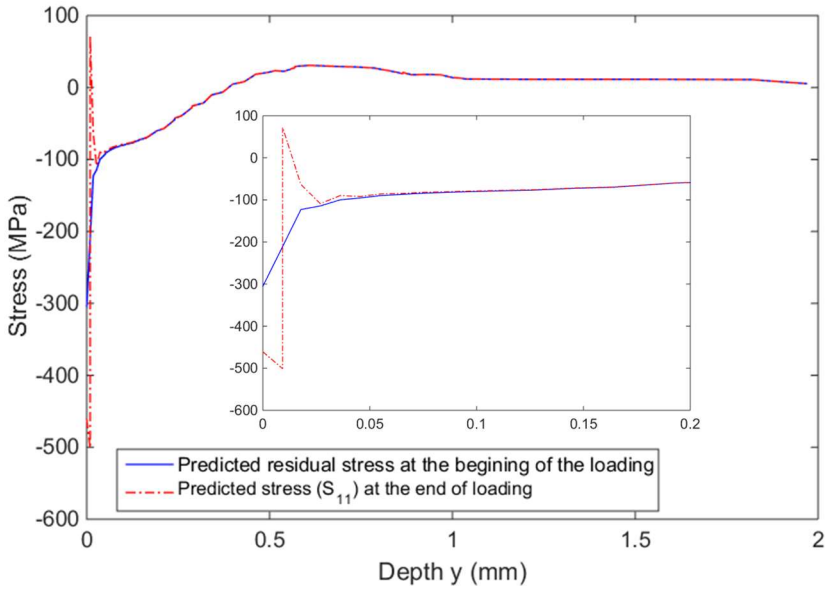

Fig. 15. The predicted residual stress distribution at the beginning of the loading and the stress distribution at the end of loading without peak load and with stress residual effect.

Further analyses are required to prove these findings, thus the residual stress relaxation for different overload values has been considered with residual stress values -80 MPa and -320 MPa induced in the material during manufacturing processes. Figure 16a-b shows the stress distribution at different step time of the loading for various peak stress magnitudes with residual stress -80 MPa and -320 MPa, respectively. With increased value for the residual stress (-320 MPa), it is observed that the residual stress relaxation rate is decreased significantly in comparison with the other case with stress residual effect -80 MPa. Figure 17 shows the effective time of residual stress before being relaxed at overload $-1.15\ S_y$ with residual stress -80 MPa and -320 MPa. It can be seen for residual stress -80 MPa, the residual stress relaxation occurs at the step time corresponding to $-0.55\ S_y$ while for residual stress -320 MPa the residual stress relaxation takes place later at the step time corresponding to $-0.95\ S_y$.

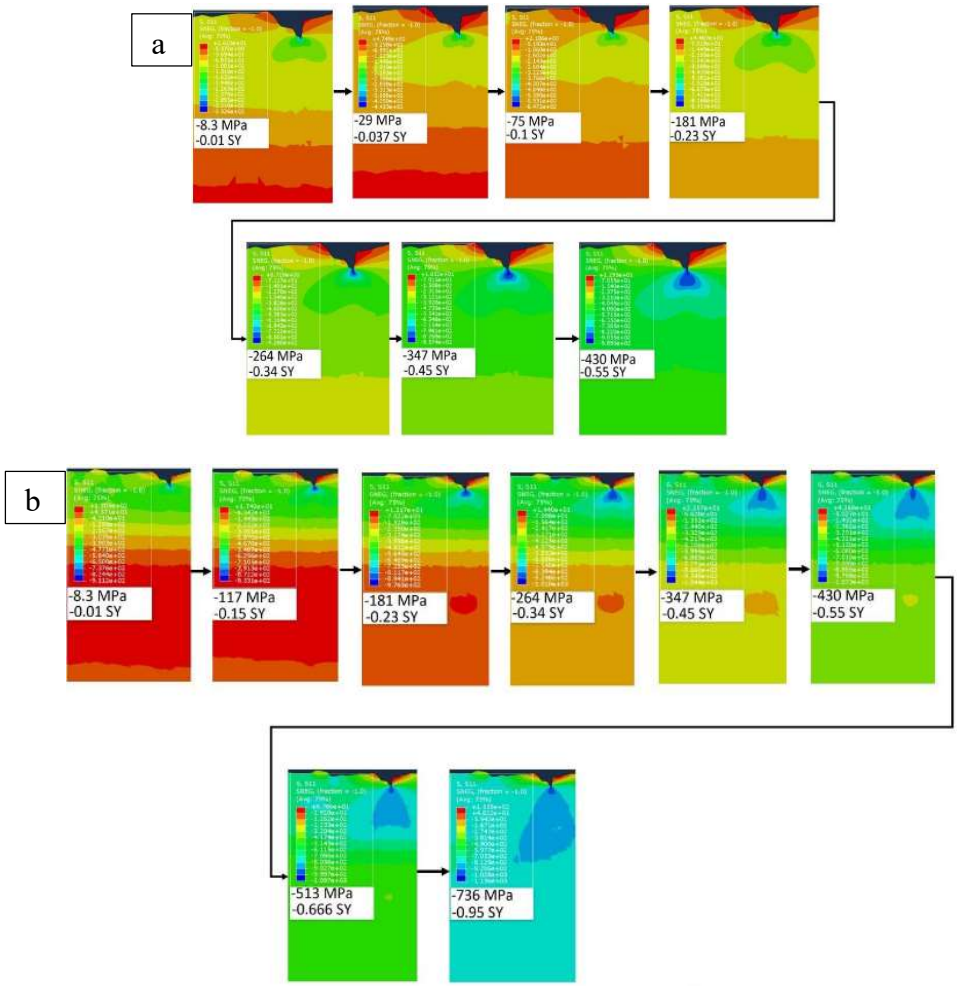

Fig. 16. The stress distribution at different step time of the loading for overload magnitude $1.15S_y$ until relaxation of the residual stress, (a) with residual stress -80 MPa and (b) with residual stress -320 MPa.

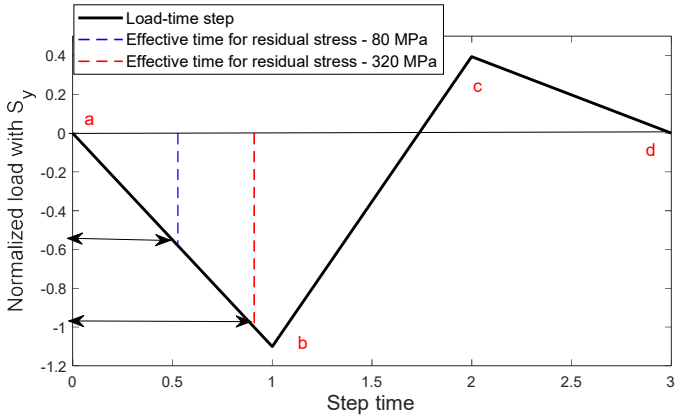

Fig. 17. Effective time for different residual stress values before being relaxed with overload $-1.15\ S_y$.

3.3 Influence of fracture locus and load level on micro crack formation

The role of material constants (C_1, C_2, C_3) on the ductile fracture criterion has been studied before [25]. As discussed, C_2 is the most affecting material constant in the ductile fracture criterion. Parameter C_2 determines the equivalent plastic strain to fracture at negative stress triaxiality in the fracture locus. In this section, the effect of C_2 and overload on the crack formation have been investigated. The other material constants C_1 and C_3 have been considered 4 and 1.2, respectively. Figure 18a-b shows the crack size at the most critical notch versus different C_2 values and their corresponding fracture locus with overload values $-1.1S_y$ and $-1.15S_y$, in the cases of two different residual stress values -80 MPa and -320 MPa, respectively. This figure shows the effect of overload, C_2 parameter (fracture locus), and residual stress effects on the damage mechanism and crack size simultaneously. It can be seen the influence of the overload on the damage formation and crack size is more than the residual stress effect and there are significant differences in the crack size between overload value $-1.1S_y$ and $-1.15S_y$ for constant residual stress magnitude (-80 MPa) as shown in Fig. 18a. However, there is not considerable variance in the crack size between different residual stress magnitudes -80 MPa and -320 MPa for constant overload value as depicted in Fig. 18b. The residual stress relaxation is the main reason for this behavior.

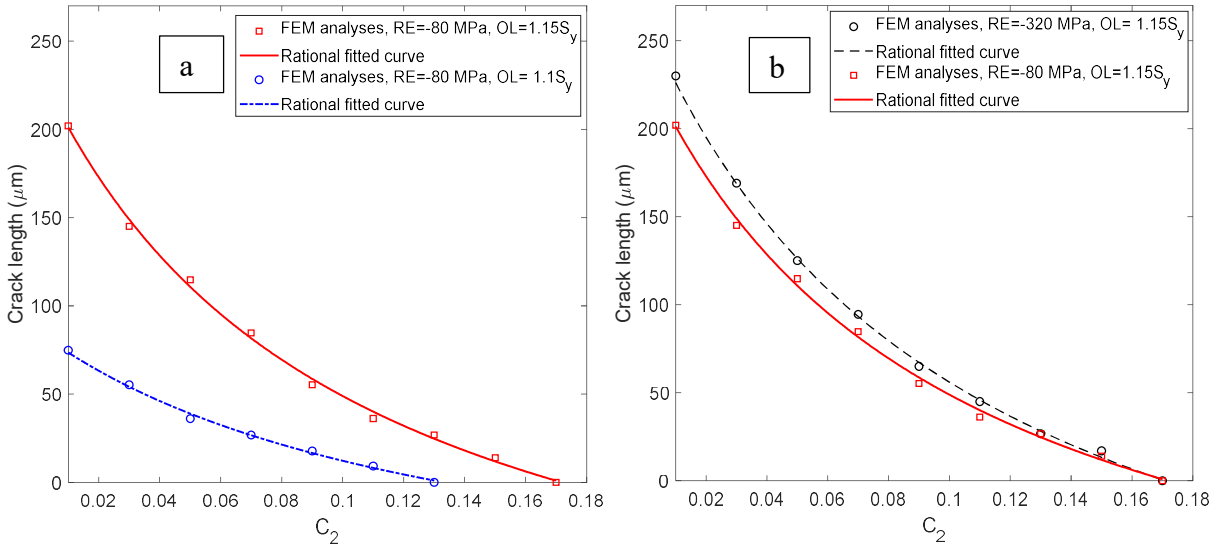

Fig. 18. Influence of (a) overload, and (b) residual stress on the damage and crack size with C_2 parameter effect simultaneously.

To further study the effect of the overload, five different peak stress magnitudes from $-0.95S_y$ to $-1.15S_y$ have been considered and the crack sizes for $C_2 = 0.01$ and $C_2 = 0.03$ with residual stress -80 MPa have been presented in Fig. 19. It can be seen there is no damage for overload values lower than $-1S_y$ and the crack sizes have been developed exponentially with increasing overload values.

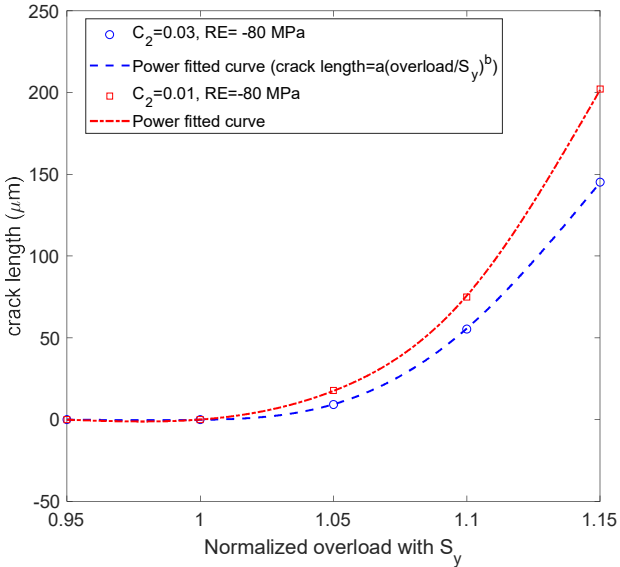

Fig. 19. Crack length versus overload values with different C_2 parameter, 0.01 and 0.03.

To clarify the influence of surface integrity when peak load is subjected on the surface as a part of loading before other fatigue loading scenario, the behavior of different elements located close to and far from the crack (see Fig. 20a) has been studied during loading time step (see Fig. 20b) for three different peak stress magnitudes as depicted in Fig. 21a-c. It can be seen the element located close to the crack (element number 2) experienced high stress at step time 3, c point of force-time profile, however, the force magnitude subjected to the element at this stage is low. Thus, this element and the other elements located in the region close to the crack tip are prone to be damaged even with a low magnitude of loading in the other load scenario after the material is subjected to the peak load. To define the size of the effective region close to the tip of the crack, the stress magnitude at different elements in the path below the crack tip has been depicted in Fig. 22a-b for three various overload magnitudes and two different fracture locus with $C_2 = 0.01$ and $C_2 = 0.03$. This figure shows the size of the effective region close to the crack tip is more extensive for higher peak stress magnitude especially in the case that the fracture locus has lower equivalent plastic strain at the compression side when $C_2 = 0.01$.

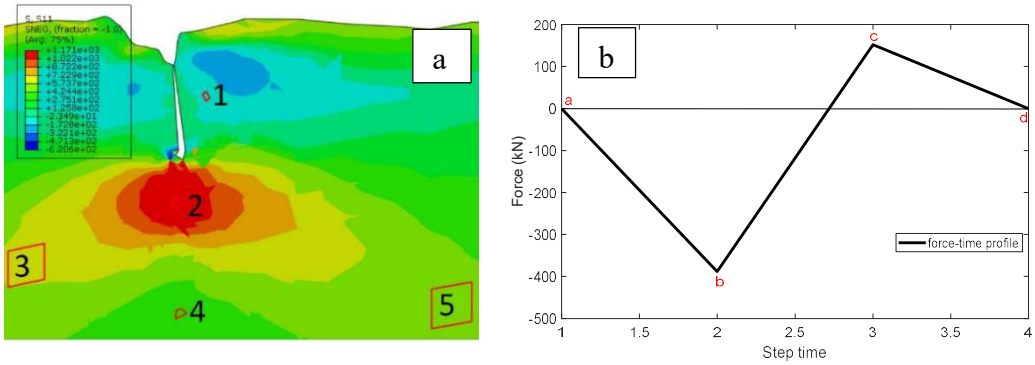

Fig. 20. (a) Locations of five different elements close and far from the crack, (b) loading time profile

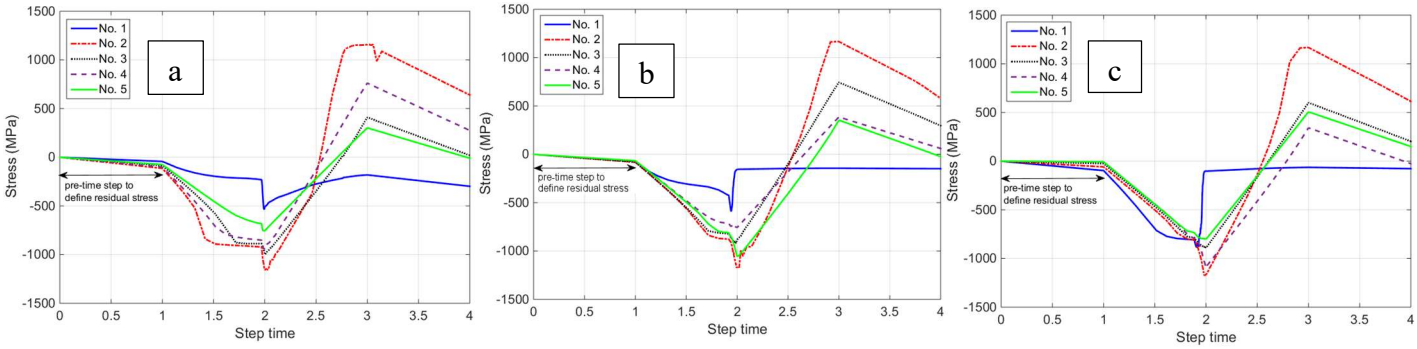

Fig. 21. Behavior of different elements located close to and far from the crack for three peak stress magnitudes, (a) $-1.05S_y$, (b) $-1.1S_y$, (c) $-1.15S_y$.

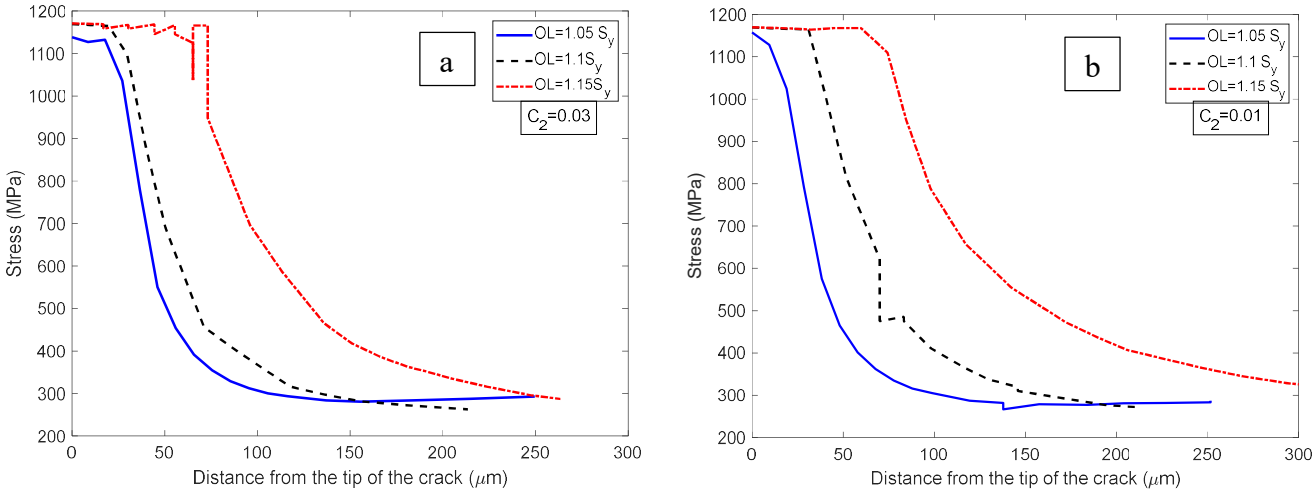

Fig. 22. Stress distribution along the path below the tip of the crack for (a) $C_2 = 0.03$ and (b) $C_2 = 0.01$ with residual stress -80 MPa.

This study additionally established new research on the influence of surface integrity when peak load is affected on the surface before or during fatigue loading. The existing analytical approach for cut-plate edges as well as welded joint utilized original geometry as an initial point for fatigue assessment while the possible influence of peak load on the geometrical parameters, residual stress state, and microcrack formation has been neglected [32-34]. The finding of this study highlights this fact that considering original geometry without

investigating the possibility of microcrack formation when peak load is a part of the loading scenario can lead to significant inaccuracy in fatigue life prediction. The amount of inaccuracy depends on the peak load magnitude. Since it has been found in this study that the crack size is developed exponentially with increasing peak load magnitudes, this neglecting may cause catastrophic problems especially when engineering components are subjected to high peak stresses and overloads during normal operation and in severe conditions. It should be noted that the present study is focused on numerical investigations of the surface integrity and its influence on the microcrack formation of sandblasted high strength steel under peak load conditions. In future work, further analysis considering experimental aspects will be carried out in real engineering situations to highlight the importance and effectiveness of the proposed numerical approach.

4 Conclusion

In this study, a new FEM approach and simulations have been employed to characterize the peak load effect on the microcrack formation and residual stress state. The numerical simulations accounted for the influences of the surface roughness and residual stress simultaneously on the performance of high strength steel under overload condition with ductile fracture criterion. By utilizing this approach, it is possible to monitor and evaluate the residual stress relaxation in real time. The main findings of this investigation can be concluded as follows

- With the increasing value of the residual stress, the residual stress relaxation rate is decreased significantly in comparison with the other studied case with lower stress residual magnitudes. The residual stress relaxation rate is an affecting parameter on

the damage mechanism and the crack size increased with a lower residual relaxation rate.

- The influence of compressive overload on the damage formation and crack size is more than the residual stress effect and there are significant differences in the crack size between various overload values for constant residual stress magnitude. However, there is not considerable variance in the crack size between different residual stress magnitudes for a constant overload value. It is found the crack size has been developed exponentially with increasing peak load magnitudes.

- Material area located in the close region to the crack tip is prone to be damaged even with a low magnitude of loading in the other load scenarios after the material is subjected to the peak load. The size of the effective region close to the crack tip is more extensive for higher peak stress magnitude especially in the case that fracture locus has lower equivalent plastic strain at the compression side.

Acknowledgement

The present research was financially supported by project RAMSSES that has received funding under the European Union's Horizon 2020 research and innovation program under the grant agreement No 723246. The information contained herein reflects the views only of the authors, and the European Union cannot be held responsible for any use which may be made of the information contained herein. All financial support is gratefully appreciated.

References

[1] Diekhoff P, Hensel J, Nitschke Th, Dilger K. Investigation on fatigue strength of cut edges produced by various cutting methods for high-strength steels. Weld World 2020;64:545-561.

[2] Sperle J O, Influence of parent metal strength on the fatigue strength of parent material with machined and thermally cut edges. IIW Document XIII-2174-07. International Institute of Welding, 2007, Paris.

[3] Alhussein A, Capelle J, Gilgert J, Tidu A, Hariri S, Azari Z. Static, dynamic and fatigue characteristics of the pipeline API 5L X52 steel after sandblasting. Eng Fail Analy 2013;27:1-15.

[4] McKelvey SA, Fatemi A. Surface finish effect on fatigue behavior of forged steel. Int J Fatigue 2012; 36(1):130–45.

[5] Hussain K, Wilkinson D, Embury J. Effect of surface finish on high temperature fatigue of a nickel based super alloy. Int J Fatigue 2009;31(4):743–50.

[6] Murakami Y, Endo M. Effect of defects, inclusions and inhomogenities on fatigue strength. Int J Fatigue 1994;16(3):163–82.

[7] Sasahara H. The effect on fatigue life of residual stress and surface hardness resulting from different cutting conditions of 0.45%C steel. Int J Mach Tools Manuf 2005;25:131–6.

[8] Ryu HR, Kim WS, Ha HI, Kang SW, Kim MH. Effect of toe grinding on fatigue strength of ship structure. J Ship Prod 2008;24(3):152–60

[9] Xun LI, Guan C, Zhao P. Influences of milling and grinding on machined surface roughness and fatigue behavior of GH4169 superalloy workpieces. Chin J Aeronaut 2018(6).

[10] Zhang M, Wang WQ, Wang PF, et al. The fatigue behavior and mechanism of FV520B-I with large surface roughness in a very high cycle regime. Eng Fail Anal 2016;66:432–44.

[11] Lopes HP, Elias CN, Vieira MV, et al. Influence of surface roughness on the fatigue life of nickel-titanium rotary endodontic instruments. J Endod 2016;42(6):965–8.

[12] Pegues J, Roach M, Scott Williamson R, et al. Surface roughness effects on the fatigue strength of additively manufactured Ti-6Al-4V. Int J Fatigue 2018;116:543–52.

[13] Novovic D, Dewes RC, Aspinwall DK, Voice W, Bowen P. The effect of machined topography and integrity on fatigue life. Int Jour Machi Tools Manufa 2004;44:125–134.

[14] Haghshenas A, Khonsari MM. Damage accumulation and crack initiation detection based on the evolution of surface roughness parameters. Int J Fatigue 2018;107:130–144.

[15] Gao Y, Li X, Yang Q, Yao M. Influence of surface integrity on fatigue strength of 40CrNi2Si2MoVA steel. Mater Lett 2007;61:466–9.

[16] Remes H, Korhonen E, Lehto, P., Romanoff J, Ehlers S, Niemela A, Hiltunen P, Kotakanen T, Influence of surface integrity on fatigue strength of high-strengh steel. J Constr Steel Res 2013; 89: 21-29.

[17] Lillemae-Avi I, Liinalampi s, Lehtimalil E, Remes H, Lehto P, Romanoff J, Ehlers S, Niemela A, Fatigue strength of high strength steel after shipyard production process of plasma cutting, grinding and sandblasting. Weld World 2018;62:1273-1287.

[18] Bao YB, Wierzbicki T. On fracture locus in the equivalent strain and stress triaxiality space. Int J Mech Sci 2004;46:81–98.

[19] Papasidero J, Doquet V, Mohr D. Ductile fracture of aluminum 2024-T351 under proportional and non-proportional multi-axial loading: Bao–Wierzbicki results revisited. Int J Solids Struct 2015;69-70:459–474.

[20] Lou Y, Huh H. Prediction of ductile fracture for advanced high strength steel with a new criterion: Experiments and simulation. J Mater Process Tech 2013;213:1284–1302.

[21] Kõrgesaar M, Romanoff J, Remes H, Palokangas P. Experimental and numerical penetration response of laser-welded stiffened panels. Int J Impact Eng 2018;114:78–92.

[22] Hu Q, Li X, Han X, Chen J. A new shear and tension based ductile fracture criterion: Modeling and validation. Eur J Mech A-Solids 2017;66: 370-386.

[23] Mohr D, Marcadet SJ. Micromechanically-motivated phenomenological Hosford–Coulomb model for predicting ductile fracture initiation at low stress triaxialities. Int J Solids Struct 2015;67-68:55.

[24] Brünig M, Albrecht D, Gerke S. Modeling of ductile damage and fracture behavior based on different micromechanisms. Int J Damage Mech 2011; 20: 558-577.

[25] Nafar Dastgerdi J, Sheibanian F, Remes H, Lehto P, Hosseini Toudeshky H. Effects of surface roughness and residual stress on the micro-crack formation. J Constr Steel Res 2020; Under Review.

[26] Lou Y, Huh H, Lim S, Pack K. New ductile fracture criterion for prediction of fracture forming limit diagrams of sheet metals. Int J Solids Struct 2012;49:3605-15.

[27] McClung RC. A literature survey on the stability and significance of residual stresses during fatigue. Fatigue Fract Eng Mater Struct 2007;30:173–205.

[28] Dalaei K, Karlsson B, Svensson LE. Stability of shot peening induced residual stresses and their influence on fatigue lifetime. Mater Sci Eng 2011;A528:1008–15.

[29] Farajian-Sohi M, Nitschke-Pagel T, Dilger K. Residual stress relaxation of quasi-statically and cyclically-loaded steel welds. Weld World 2010;54:49–60.

[30] Laamouri A, Sidhom H, Braham C. Evaluation of residual stress relaxation and its effect on fatigue strength of AISI 316L stainless steel ground surfaces: Experimental and numerical approaches. Int J Fatigue 2013;48:109-121.

[31] SFS-EN ISO 4288. Geometrical Product Specifications (GPS) — surface texture: profile method — rules and procedures for the assessment of surface texture; 1996.

[32] Lestari S. Residual stress measurements of unblasted and sandblasted mild steel specimens using X-Ray diffraction, strain-gage hole drilling, and electronic speckle pattern interferometry (ESPI) hole drilling methods" (2004). University of New Orleans Theses and Dissertations. 90.

[33] Hoa HC , Chunga KF, Liua X, Xiaoa M , Nethercot DA. Modelling tensile tests on high strength S690 steel materials undergoing large deformations. Eng Struct 2019;192:305-322.

[34] Radaj D, Sonsino CM, Fricke W. Recent developments in local concepts of fatigue 26 assessment of welded joints. Int. J. Fatigue 2009; 31:2-11.

[35] Arola D, Ramulu M. An examination of the effects from surface texture on the strength of fiber reinforced plastics. J Compos Mater 1999;33(2):102–23.

[36] Arola D, Williams CL. Estimating the fatigue stress concentration factor of machined surfaces. Int J Fatigue 2002;24(9):923–30.